DOI: 10.13009/EUCASS2022-6178
9TH EUROPEAN CONFERENCE FOR AERONAUTICS AND SPACE SCIENCES (EUCASS)

Design of multiscale inhomogeneous grids for the generation of atmospheric boundary layer logarithmic mean flows

HURET Thomas[1], TANGUY Geoffrey[1], VASSILICOS Christos[1], JACQUIN Laurent[2] and GALLAS Quentin[3]*

[1]Univ. Lille, CNRS, ONERA, Arts et Métiers Institute of Technology, Centrale Lille, UMR 9014 – LMFL – Laboratoire de Mécanique des Fluides de Lille – Kampé de Fériet, F-59000 Lille, France
**thomas.huret@onera.fr*

[2]DAAA, ONERA, Université Paris-Saclay, F-92190 Meudon - France

[3]ONERA–The French Aerospace Lab, 31410 Mauzac, France

Abstract

Wind tunnel generation of flows representative of the Atmospheric Boundary Layer (ABL) still requires trial-and-error based design processes for both passive and active devices. To address this issue, a new type of passive grids – Multiscale Inhomogeneous Grids (MIGs) — is presented. It takes advantage of obstruction variations and interacting wakes to tailor both mean flow profile and turbulent intensity profiles downstream the grid.
The present work derives theoretical models in order to predict the mean velocity profile of MIG-generated flows characteristics for applications to neutral atmospheric boundary layer. These prediction models are investigated experimentally downstream of MIGs using Hot-Wire Anemometry within the SCL-PIV subsonic wind tunnel at ONERA Lille (Section $H \times W = 290mm \times 300mm$, velocities up to $30\ m/s$).
First, the mean velocity profile prediction, based on McCarthy (1954), is applied with MIGs to generate logarithmic mean profiles for an equivalent roughness length h_0 consistent with the characterized roughness of LEGO® baseboard surface. The interaction of these grid-generated flows with artificial roughness is then investigated, showing a good fit in the central region, yet revealing clear discrepancies in the wall-affected region, contrary to past boundary layer generating devices, such as spires. The study concludes on the need for further understanding of the turbulence characteristics of the generated flows, also mandatory for the current development of a turbulence prediction model.

1. Introduction

1.1 The Atmospheric Boundary Layer (ABL) in wind tunnel

The experimental generation of wind tunnel flows representative of the Atmospheric Boundary Layer (ABL) has been investigated during the last decade of the 20th century with both passive [1-4] and active devices [5]. Similarity criteria were derived by Cermak (1971) [6] and Avissar *et al.* (1990) [7] who emphasized the impossibility of reaching a configuration fully similar to the atmospheric case. Attempts of reproducing the ABL in wind tunnels are therefore focused on the reproduction of the main flow characteristics. Armitt & Counihan (1968) [8] reviewed the wind engineering requirements depending of the application (e.g. civil engineering or pollutant dispersal) and listed the flow characteristics of interest to be mainly the vertical profiles of mean velocity, turbulence intensity components and turbulence integral length scales.

The roughness similarity criteria by Jensen & Franck (1963) [9] is of significant importance for the reproduction of these flow quantities, especially close to the wall. It states that the Jensen number $Je = h_0/D$ should be conserved between the wind tunnel and the represented atmospheric configuration, where h_0 stands for the "roughness length" and D represents either the boundary layer depth (if fully reproduced in wind tunnel) or the wind tunnel full height (if only part of the boundary layer is reproduced within the full wind tunnel section).

DOI: 10.13009/EUCASS2022-6178

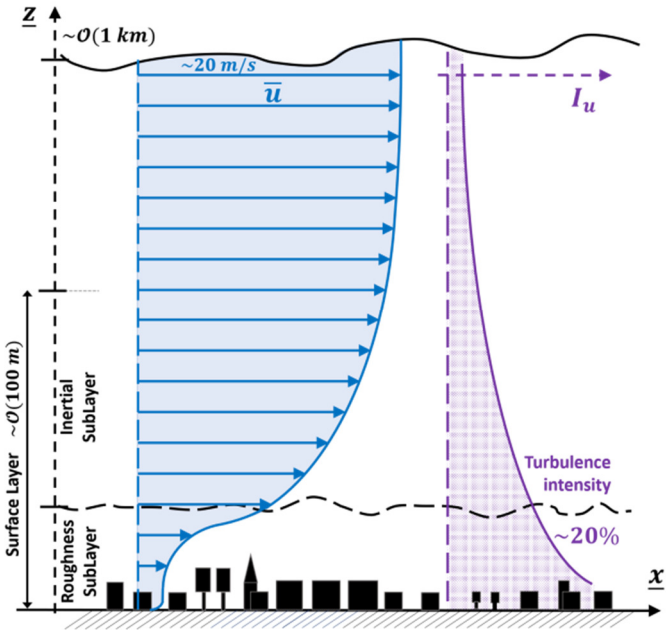

Figure 1: Schematic visualization of the neutral Atmospheric Boundary Layer. Based on [10][11].

The wind tunnel configurations studied in this work are representative of neutral ABL over flat surfaces of homogeneous roughness, quantified by the "roughness length" h_0. This quantity is defined through the mean velocity profile obtained in the Inertial SubLayer (ISL) of the ABL, characterized by a logarithmic dependency with the altitude [10] (see Figure 1), as described by the equation:

$$\overline{u}(z) = \frac{u_*}{\kappa} \ln\left(\frac{z-d}{h_0}\right) \tag{1}$$

The friction velocity u_* is defined as $u_* := \sqrt{\frac{\tau_{friction \to wall}}{\rho}} \approx \sqrt{-\langle u'w' \rangle_{wall}}$. This behaviour is analogous to the log-law observable within classic rough-wall turbulent boundary layer, since the ABL is equivalent to such flow in case of negligible vertical heat flux (neutral ABL) [12].

At high Reynolds number, the roughness length is a function of the roughness elements geometry only [12]. Classifications were suggested [15, 16] to relate a class of terrain to a roughness length, leading to a range of h_0 between $0.0003\ m$ and $2\ m$ for the revised Davenport's classification (2000).

Davenport & Isyumov (1967) [15] showed that the best available device to reproduce a full ABL is the natural growth of a turbulent boundary layer over a roughness fetch long of about 25 to 35 the depth of the desired boundary layer. Such high aspect ratio is in general out of reach for most of the aerodynamic wind tunnels in use, therefore, the next devices were attempting to reduce this development length by artificially thickening the boundary layer. In particular, the Counihan-type configurations [1, 18] were successful in reproducing the atmospheric mean flow profile and correct profiles of turbulence intensities. Inspired by this device, Cook (1978) [3] presented a family of configurations and suggested a general understanding of the behaviour of such devices, named as "roughness-barrier-mixing device method" (RBM).

DOI: 10.13009/EUCASS2022-6178

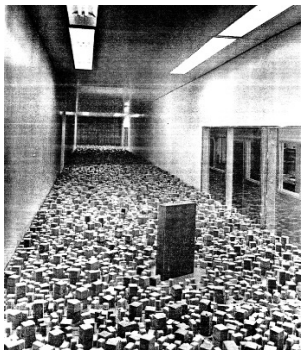

(a) Davenport & Isyumov (1967) [15]

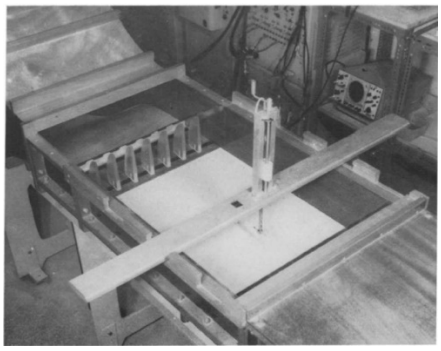

(b) Counihan (1969) [1]

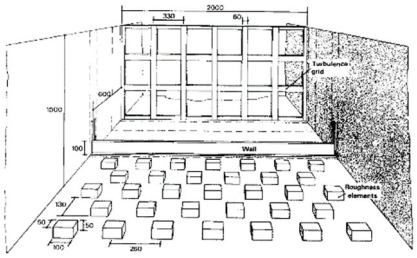

(c) Cook (1978) [3]

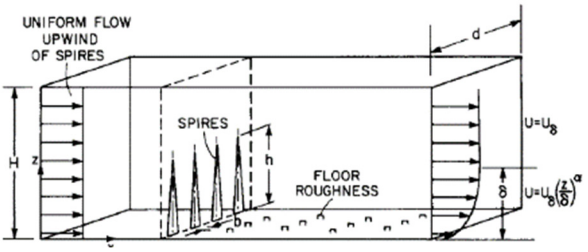

(d) Irwin (1981) [4]

Figure 2: Several passive devices for the generation of a neutral ABL in wind tunnel

However, such devices are designed by trial-and-error for a given atmospheric flow of interest (i.e. for a given roughness). Such trial-and-error process must be reproduced for each new studied configuration and each new wind tunnel setup.

This was observed by Cook (1978) [3] who undertook a parametric analysis on their devices to relate the effective roughness length and integral length scales to their geometric parameter (the height of the wall component, see Figure (2c)).

Irwin (1981) [4] summarized a successful attempt to tailor the mean flow profile (not the turbulent intensity profile) using a simple geometry ("spires" and roughness) related to the downstream mean flow characteristics by empirical and theoretical models [17]. These technics are widely used by both research and industrial communities, even though it cannot tailor turbulence intensity independently of mean flow profile.

1.2 Objectives

The present work aims at reproducing experimentally a logarithmic mean flow by associating roughness and a recently introduced passive grid device. Such configuration is thought to be representative of the atmospheric Surface Layer (see Figure 1). Multiscale Inhomogeneous Grids are passive devices introduced recently by Zheng et al (2018) [18]. Their design is expected to enable tailoring (without trial-and-error) both mean flow profile and turbulent intensity profiles, by taking advantage of tools developed initially for fractal grids studies.

The next section presents the past work establishing ways to design a grid for a given mean flow profile.

2. Multiscale Inhomogeneous Grids (MIGs) design

2.1 Multiscale Inhomogeneous Grids

Multiscale Inhomogeneous Grids [18] are composed of regular arrays of vertical bars within several horizontal levels of varying geometric properties (w_n, g_n, h_n, see Figure 3).

DOI: 10.13009/EUCASS2022-6178

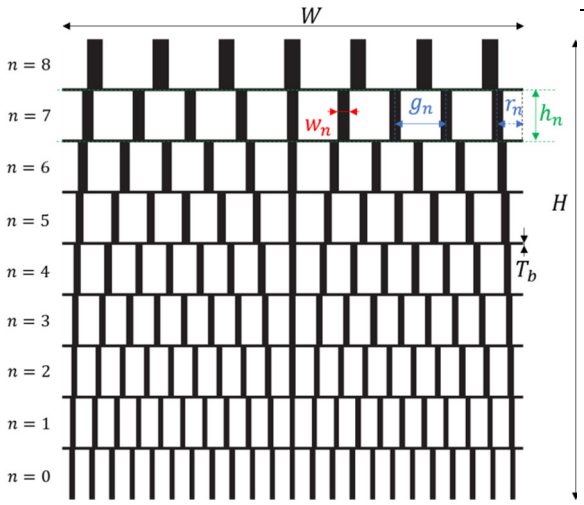

Figure 3: Several passive devices for the generation of a neutral ABL in wind tunnel

Notation	Definition
N	Number of layers
W	Width of the grid section
H	Height of the grid section
T_b	Width of the horizontal bars
d_b	Streamwise depth of the horizontal bars
h_n	Height of each layer (horizontal Bars center to center)
g_n	Distance between adjacent vertical bars (center to center)
r_n	Distance from the wall of the first vertical bar of the level
w_n	Width of vertical bars
d_n	Streamwise depth of vertical bars
c_n	Number of vertical bars
σ_n	Blockage ratio (solidity) of the layer

Table 1: Definition of the different geometric parameters of MIG grid.

At each level n, the number of vertical bars can be computed from the other geometrical quantities $\frac{W}{2} = \frac{c_n - 1}{2} g_n + r_n$ with $0 \leq r_n < g_n$ and c_n an odd natural number

Assuming that the lateral walls of the wind tunnel act as mirrors for the flow, the choice $r_n = \frac{g_n}{2}$ theoretically minimizes the boundary effects that could occur, by mimicking an infinitely periodic set of vertical bars.
Each level is finally characterized by its local blockage ratio (i.e. ratio between the filled area and the total area of the level), computed as:

$$\sigma_n = \begin{cases} \dfrac{c_n w_n (h_n - T_b) + T_b W}{h_n W} & \text{for n } \in [|1, N-2|] \\ \dfrac{c_n w_n (h_n - T_b) + \frac{1}{2} T_b W}{\left(h_n - \frac{1}{2} T_b\right) W} & \text{for } n = 0 \text{ or } n = N-1 \end{cases}$$

2.2 Theoretical prediction of the mean flow profile

The MIGs are composed of multiple horizontal layers, each of them harbouring an array of vertical bars of the same width. Width and distance between two vertical bars are dependent of the grid level. The non-uniform local blockage ratio that is produced generates a non-uniform pressure jump between the two sides of the grid. This pressure jump, normalized as $K = (P_{0-} - P_{0+})/\frac{1}{2}\rho u_0^2$ in the following, produces a non-uniform pressure field upstream and downstream, both of which influencing the mean flow velocity. The grid geometry is therefore a way to convert the far upstream mean flow distribution $u^{-\infty}$ into a sheared mean flow far downstream $u^{+\infty}$ (see Figure 3).

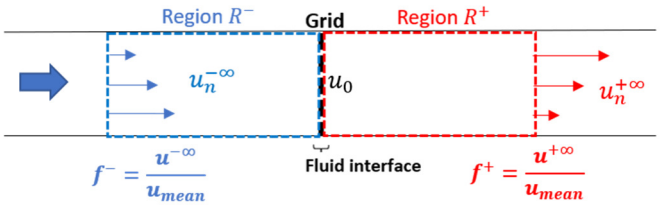

Figure 4: Schematic visualization of the regions of influence of the grid upstream and downstream within the wind tunnel. Inspired from [19]

The influence of the blockage ratio of a uniform gauze on the flow features has been studied first by Taylor *et al.* (1949) [20]. Owen & Zienkiewicz (1957) [21] explored the possibilities of producing a uniform shear flow using a

DOI: 10.13009/EUCASS2022-6178

non-uniform local blockage ratio distribution. The theoretical reasoning was further developed by Elder (1959) [22] and then by McCarthy (1964) [19], reaching an equivalent formulation of the same equation model (see Equation (2)), but studied with two different sets of assumptions. As summarized in McCarthy (1964) [19], the reasoning is derived with the assumptions that: (i) the grid is a fluid interface out of which viscosity effects are negligible, (ii) the Reynolds stresses are neglected in the Reynolds-Averaged Navier Stokes (RANS) equation, (iii) the deflection of streamlines is negligible (i.e. $\overline{v} \ll \overline{u}$ and $\overline{w} \ll \overline{u}$) and (iv) the resulting mean flow has no swirling components.

$$\left(\left[\frac{B}{\chi^2}\frac{\chi^2-1}{\left(1+\frac{B}{\chi}\right)^2}+\frac{\chi}{1+\frac{B}{\chi}}\right]\left(u^{+\infty}+\frac{B}{\chi}u^{-\infty}\right)-\frac{B}{\chi^2}\frac{\chi^2-1}{1+\frac{B}{\chi}}u^{-\infty}\right)d\chi+\left(1+\frac{\chi^2-1}{1+\frac{B}{\chi}}\right)du^{+\infty}+\left(\frac{\frac{B}{\chi}(\chi^2-1)}{1+\frac{B}{\chi}}-1\right)du^{-\infty}=0 \quad (2)$$

Where: $\chi=\sqrt{1+K}$ is associated to the grid-generated pressure jump distribution and $B\sim1.1$ is a constant empirically deduced by Taylor *et al.* (1949) [20] in order to relate the pressure jump K and the deflection coefficient α by the expression $\alpha=B/\sqrt{1+K}$. There is no clear consensus on the relation between K and the grid geometry, even though several empirical laws were suggested to relate it to the grid local blockage ratio (see for instance Karnik & Tavoularis 1987 [23]). McCarthy (1964) [19] considered the Equation (3) coming from Wieghardt (1953) [24], with a coefficient r depending on the interstitial Reynolds number $Re_i=u_0 w/((1-\sigma)\nu)$ with w the width of the considered grid bar.

$$K=\frac{r\sigma}{(1-\sigma)^2} \quad (3)$$

McCarthy (1964) [19] considered the value of $r=0.78$ while Zheng et al (2018) [16] preferred $r=0.7$, observed by Cornell (1958) [25] up to $Re_i=4\times10^4$ (typical values in our cases lie between 10^3 and 10^4). Another formulation is given by Roach (1987) [26] in Equation (4).

$$K=A\left(\frac{1}{(1-\sigma)^2}-1\right)^B \quad (4)$$

The parameters A and B depends on the Reynolds number and the grid bars/mesh geometry. Roach (1987) [26] estimated them experimentally for different grids configuration by changing both the mesh (parallel bars or square mesh) and the grid bars geometry (square or circular sections). It appears that the two coefficients mainly depend on the section of the bars as summarized in the Table (2).

Table 2 : Empirical estimation of coefficients for Equation (4) from Roach (1987) [26]

	Circular bars	**Square bars**
A	0.52[a]	0.98[b]
B	1.0	1.09

[a] *Valid for* $Re_w=u^{-\infty}w/\nu\in[10^2,10^5]$. *More precisely, in this range:* $A=0.52+66/Re_w^{4/3}$. *Typical range for the present work is* $Re_w\in[10^3,10^4]$.
[b] *Valid for* $Re_w=u^{-\infty}w/\nu\in[10^2,10^4]$. *Negligible dependency with* Re_w *in this range. Typical range for the present work is* $Re_w\in[10^3,10^4]$.

It can be shown from the results by [26] that the Equation (3) is more relevant for the study of grids with circular bars, since Equation (3) and (4) are giving similar values. On the contrary, square bars case gives a relation different by a factor around 2. The next experimental results demonstrate that the Equation (4) with "square bars" parameters gives correct prediction of the MIG-generated mean flows, contrary to circular bars parameters or Equation (3). Therefore, the Equation (4) with square bars case is implicitly kept in the following analysis.

DOI: 10.13009/EUCASS2022-6178

McCarthy (1964) model

McCarthy (1964) [19] considered the far upstream flow to be perfectly homogeneous ($du^{-\infty} = 0$ and $u^{-\infty} = u_{mean}$) so that the Equation (2) becomes a non-linear Ordinary Differential Equation on $u^{+\infty}$ as a function of χ. This equation was solved analytically by approximating several integrals up to the second order (see [19]). The resulting relation between normalized mean flow profile and normalized pressure jump is given in Equation (3) for a problem discretized over the N levels of the designed grid.

$$f_n^+ = 1 - 1{,}01\mathcal{A}(K_n)(\mathcal{B}(K_n) - \gamma_n) \tag{5}$$

With
$$\mathcal{A}(K_n) = \frac{1+\sqrt{1+K_n}}{\left(1+(1+K_n)^{3/2}\right)^{2/3}}$$
$$\mathcal{B}(K_n) = \frac{\frac{1}{6}+(1+K_n)^{3/2}}{1+K_n}$$
$$\gamma(\{K_n\}_n) = \frac{\sum_{n=0}^{N-1}\mathcal{A}(K_n)\mathcal{B}(K_n)h_n}{\sum_{n=0}^{N-1}\mathcal{A}(K_n)h_n}$$

This non-linear coupled equation system is inverted by a Sequential Least Squares Programming (SLSQP) algorithm in order to find the $\{K_n\}_n$ distribution that would minimize the cost function $F(\{K_n\}_n) = \sum_{n=0}^{N-1}(f_n^+ - [1 - 1{,}01\mathcal{A}(K_n)(\mathcal{B}(K_n) - \gamma_n)])^2$ for a given objective function f_n^+.

A numerical solving model

Another way to solve Equation (2) without asking for extra hypothesis on the upstream mean flow (or analytical approximations) consists in solving it numerically. For prescribed normalized upstream and downstream mean flow, Equation (2) can be rewritten as:

$$\frac{\partial\chi}{\partial z} = \frac{G_+(\chi)\frac{df^+}{dz} + G_-(\chi)\frac{df^-}{dz}}{\left[\mathcal{M}(\chi) - \frac{B}{\chi}\right]f^- - \mathcal{L}(\chi)f^+} \; and \; \chi(z=0) = \chi_0 \tag{6}$$

With
$$G_+(\chi) = 1 + \frac{\chi^2-1}{1+\frac{B}{\chi}}, \quad G_-(\chi) = \frac{\frac{B}{\chi}(\chi^2-1)}{1+\frac{B}{\chi}} - 1$$
$$\mathcal{M}(\chi) = \frac{B}{\chi^2}\frac{\chi^2-1}{1+\frac{B}{\chi}}, \qquad \mathcal{L}(\chi) = \left[\frac{B}{\chi^2}\frac{\chi^2-1}{\left(1+\frac{B}{\chi}\right)^2} + \frac{\chi}{1+\frac{B}{\chi}}\right]$$

The solution of this problem, numerically computed using a Runke-Kutta 4 (RK4) method, is then discretized over N grid levels. The final problem consists in finding the correct initial condition in order to obtain the prescribed mean blockage ratio expected over the full section. This is realized by a dichotomy algorithm.

2.3 Grid design algorithm

Using the mean flow tailoring tools described above, a grid design algorithm was implemented in two versions depending of the modelling choice. They can be visualized schematically in Figure (5) and Figure (6). Choice was made to arbitrarily fix the distance g_n between two adjacent bars and the height of each grid level, since they represent extra-degrees of freedom that will become useful only for generating prescribed turbulence profiles.

DOI: 10.13009/EUCASS2022-6178

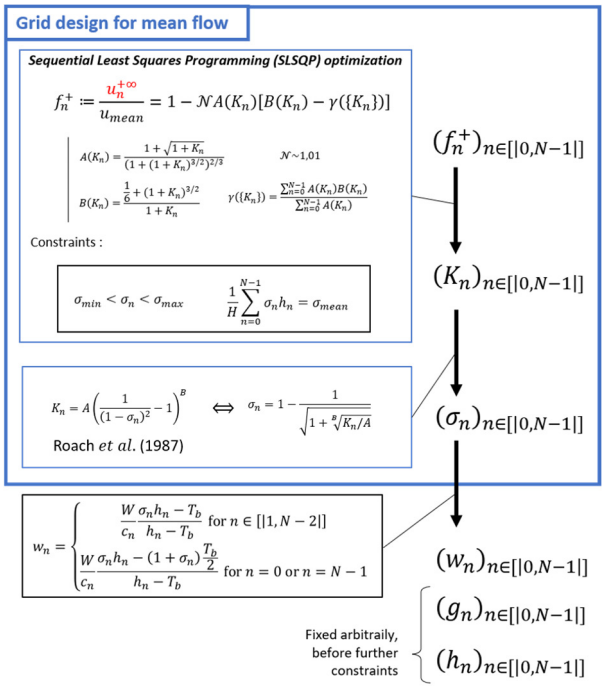

Figure 5: Schematic representation of the grid design algorithm using the McCarthy (1964) [19] model.

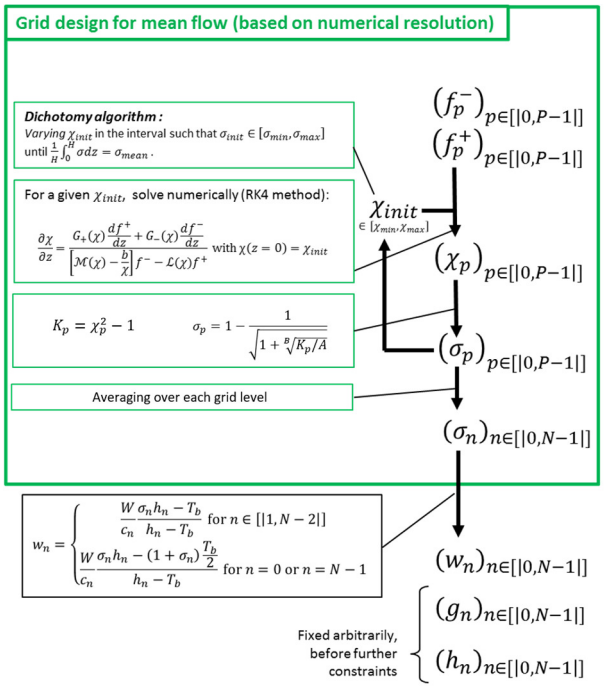

Figure 6: Schematic representation of the grid design algorithm solving Equation (2) numerically.

The design for grids dedicated to the generation of a logarithmic mean flow is fully characterized by two inputs parameters: the mean blockage ratio σ_{mean} (averaged over the full wind tunnel section area) and the non-dimensional roughness ratio h_0/H.

3. Experimental setup

3.1 Hot-wire Anemometry in SCL-PIV wind tunnel (ONERA Lille)

The SCL-PIV wind tunnel (ONERA Lille) is dedicated to boundary layer studies. The working section of $H \times W = 0.29\ m \times 0.30\ m$ enables an exploration by both Hot-Wire Anemometry (HWA) and Particle Image Velocimetry (PIV). The operational velocity range is between 10 m/s and 30 m/s.The current work presents HWA results obtained for a reference velocity of $U_{pitot} = 15\ m/s$ (global Reynolds number $Re = U_{pitot}H/\nu \sim 2.78 \times 10^5$).

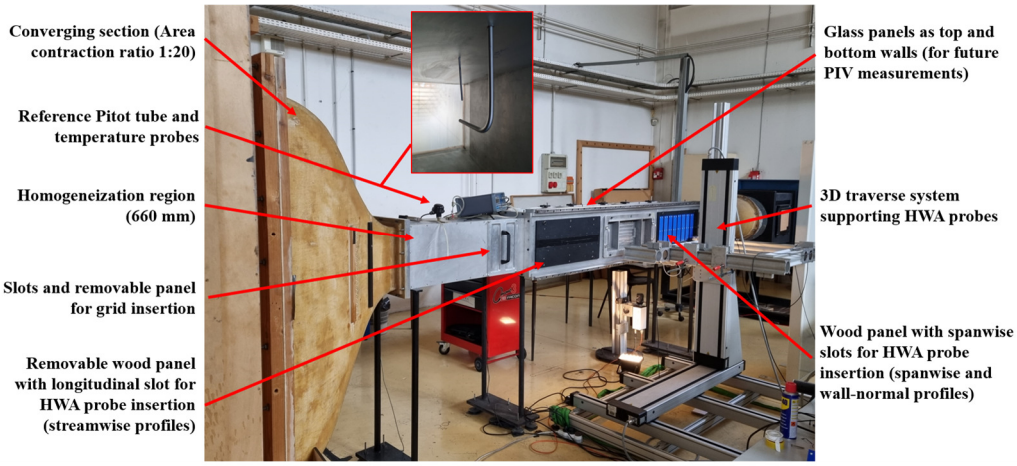

Figure 7: The SCL-PIV wind tunnel (ONERA Lille).

DOI: 10.13009/EUCASS2022-6178

The wind tunnel has the specificity to enable the easy insertion of grids through 15 mm-wide and 5 mm depth slots (see Figure (7) and Figure (8)). Upstream of this location, an empty section is dedicated to produce a homogeneous parallel flow after a 200 mm long and 10 mm high bevel. The empty vein characterization reveals boundary layers at the grid location of 10 mm high (results not shown).

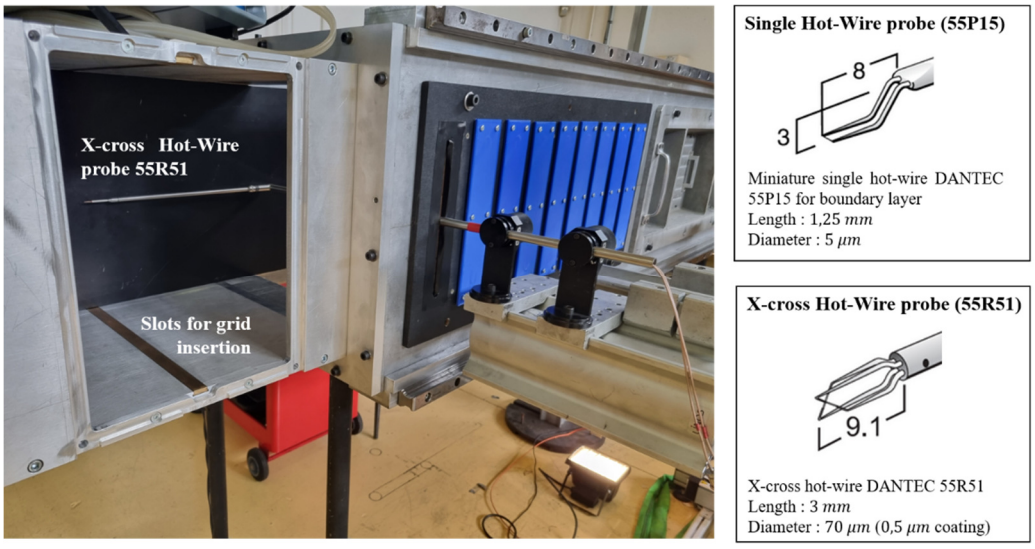

Figure 8: Hot-Wire setup inserted through a transverse slot of a removable wood panel.

Two different Hot-Wire probes are considered (see Figure (8)). A single Hot-Wire probe with frequency response up to very high frequencies for spectral studies. It also enables to reach points close to the wall. These measurements are complemented by a X-cross Hot-Wires probe leading to two velocity components and Reynolds stress measurements. For every acquisition point of the present work, a signal of 30s is acquired at $f_{acq} = 100\ kHz$. An analog low-pass filter at $f_{cutoff} = 30\ kHz$ is applied before acquisition.

Three windows enable the exploration of the flow through a total streamwise distance of 1950 mm from the grid insertion slots. These windows are occupied by adaptable wood panels with slots of different orientations depending of the required profile. The current work presents results measured across the “IIIT9-center” profile (wall_normal profile) visible in red in Figure (9).

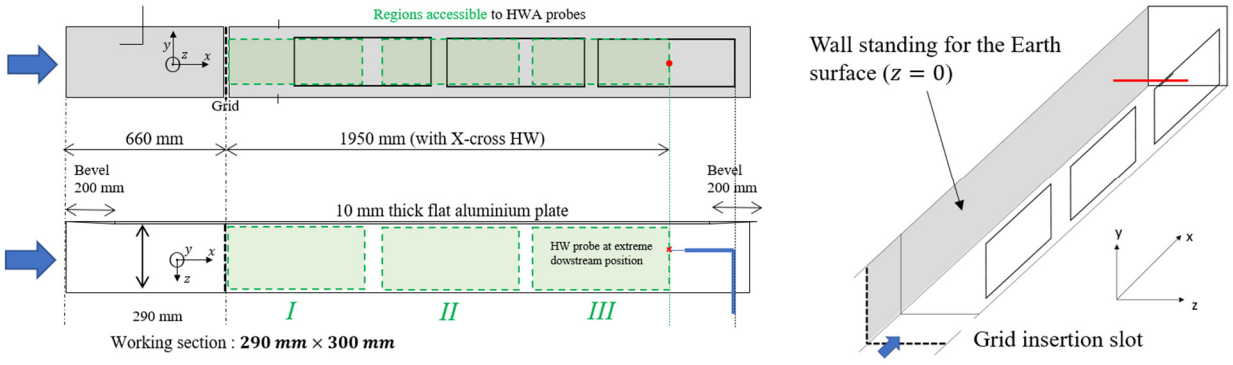

Figure 9: Schematic visualization of the wind tunnel working section. The “IIIT9-center” profile is highlighted in red

DOI: 10.13009/EUCASS2022-6178

3.2 Roughness characterisation

In order to reproduce the surface layer of the ABL (see Figure (1)), the Jensen similarity criterium requires that the "roughness length" of the considered terrain must be represented at scale in the wind tunnel. In the SCL-PIV wind tunnel, LEGO® Baseboards have been implemented on the wall to represent a high roughness configuration. The measured mean flow profiles for both flat and rough configurations are presented in Figure (11) for a reference velocity $U_{pitot} = 15\ m/s$. The extrapolated altitude of zero-velocity crossing reveals the roughness length h_0 for both cases.

(a) Smooth configuration: Aluminium flat plate

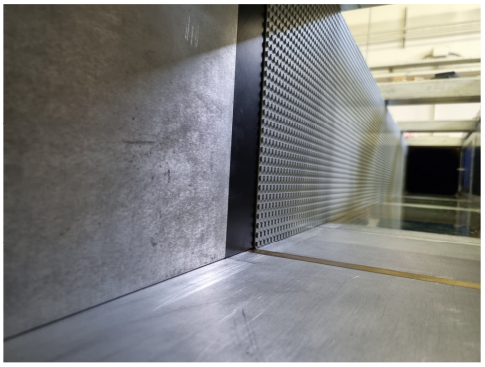

(b) Rough configuration: LEGO® Baseboard

Figure 10: The two roughness configurations. The rough case consists in LEGO® Baseboards sticked to the aluminium flat plate.

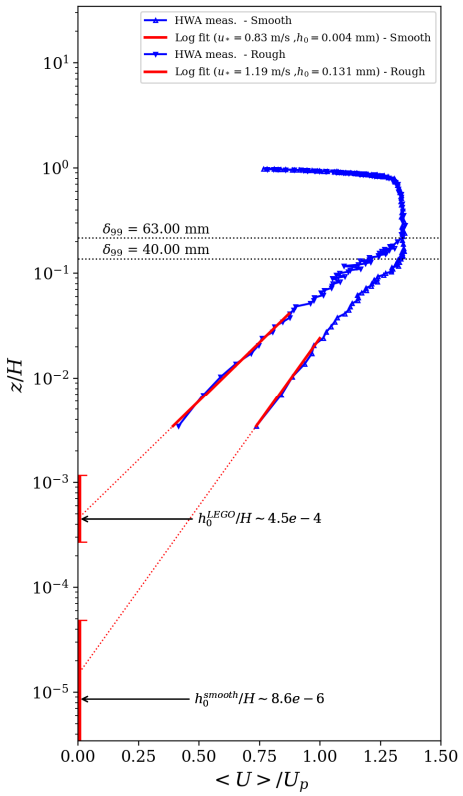

Figure 11: Measured mean streamwise velocity profile for the smooth and the rough configurations. The lowest $0.2\delta_{99}$-region is fitted using logarithmic law (red lines). The 95% confidence intervals on h_0/H estimates are plotted on the Y-axis.

Figure (11) is consistent with the expected $h_0^{smooth} = 0.0025\ mm$ [12] and $h_0^{LEGO} = 0.13$ mm [1]. Therefore, it is this value that has been chosen as an input for the logarithmic objective function that will be generated for the next sections.

3.3 Definition of the 6 grids

In the present work, six different grids were designed in order to fit within the SCL-PIV slot. A 3-side frame is added to the grid for insertion in SCL-PIV wind tunnel. It is designed in order to be flush with the wind tunnel walls. All of the grids (except the spires configuration) share the same characteristics for their horizontal bars (a width $T_b = 1.66\ mm$ and a depth $d_b = 10\ mm$). The different grids are listed in Figure (12).

The five first grids/obstacles are designed in order to generate the same objective mean flow: a logarithmic mean flow with artificial roughness $h_0^{objective}/H = 4.5 \times 10^{-4}$ (compatible with LEGO® Baseboard roughness, see Figure (11)) over the full section of the wind tunnel.

DOI: 10.13009/EUCASS2022-6178

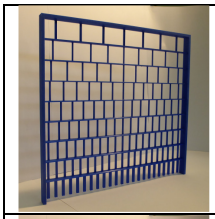	***MIG-log-LEGO_N9*** 9 levels of same height. Designed with the McCarthy model (1964) [19]. $h_0/H = 4.5 \times 10^{-4}$. $\sigma_{mean} = 0.2$ $\sigma_{max} = 0.389$	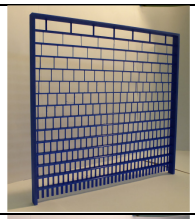	***MIG-log-LEGO_N15*** 15 levels of same height. Designed with the McCarthy model (1964) [19]. $h_0/H = 4.5 \times 10^{-4}$. $\sigma_{mean} = 0.2$ $\sigma_{max} = 0.442$
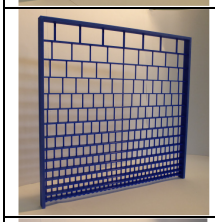	***MIGnh-log-LEGO_N15*** 15 levels of increasing height (power law of the altitude). Designed with the McCarthy model (1964) [19]. $h_0/H = 4.5 \times 10^{-4}$. $\sigma_{mean} = 0.2$ $\sigma_{max} = 0.597$	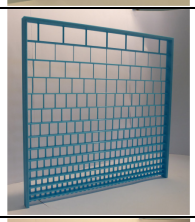	***MIGnh-rk4-log-LEGO_N15*** 15 levels of increasing height (power law of the altitude). Designed with the numerical solving (RK4) of Equation (2) [19]. $h_0/H = 4.5 \times 10^{-4}$. $\sigma_{mean} = 0.2$ $\sigma_{max} = 0.630$
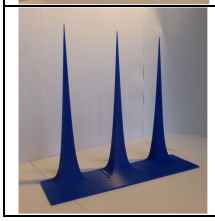	***MIG-spires-log-LEGO_N500*** 500 levels. No horizontal bar. Only three vertical bars at each level, leading to three spires. Designed with the McCarthy model (1964) [19]. $h_0/H = 4.5 \times 10^{-4}$. $\sigma_{mean} = 0.2$	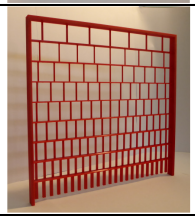	***MIG-log-1e-3_N9*** 9 levels of same height. Designed with the McCarthy model (1964) [19]. $h_0/H = 10^{-3}$. $\sigma_{mean} = 0.2$ $\sigma_{max} = 0.413$

Figure 12: Main characteristics of the 6 grids designed using the algorithm of the previous section. The grids are all 3D printed in PLA with a 100% fill.

4. Experimental investigations

4.1 Grid-alone configurations (no roughness)

The measurements by X-cross hot-wire at the "IIIT9-Center" profile (see Section 3.1) downstream of each grid is presented in Figure (13). For each plot, two different regions are visible: a wall-region of approximately the same height as the natural boundary layer growing in empty vein configuration, and a center vein region (roughly between 0.2H and 0.8H) showing a logarithmic evolution of the mean flow profile. Inspired by the flow past a change of roughness, where an inner boundary layer forms within a deeper one, the wall-affected region visible in our results is interpreted as a boundary layer naturally growing within the grid-generated flow. It is of interest to notice that the wall-affected region seems to coincide with the empty vein natural boundary layer (without grid or obstacle).

The profiles within these two regions are fitted by logarithmic laws in order to estimate their equivalent friction velocities and roughness lengths. Such estimation by interpolation of mean profile is known to suffer from large uncertainties [3], in particular for roughness measurement (due to the exponential relation between roughness length and velocity and the difficulty to access the vicinity of the wall). The 95%-confidence intervals for the estimation of the roughness length are presented as continuous vertical lines on the plots of Figure (13).

As expected, the wall-region of the profiles always reach the same very low roughness length of the smooth configuration. This observation justifies the need for a roughness similarity of the wall surface with the required value of h_0, as expressed by the Jensen similarity criterium [9]. On the contrary, the center of the vein reveals the presence of log-laws (as expected by design) with artificial h_0/H of the correct order of magnitude compared to the grid design input. Exceptions to this observation are: (a) "*MIG-log-LEGO_N9"* and (c) "*MIGnh-log-LEGO_N15"*, which shows values of artificial h_0 respectively too high and too small. These discrepancies could be explain by three reasons: (i) the 3D printing geometric uncertainties; (ii) possible imperfections of the McCarthy model; (iii) the absence of roughness similarity.

By propagating the geometric uncertainty of the 3D-printing process ($\sim 0.4\ mm$ on each geometric parameter) through Equation (2), the maximum error on the generated velocity is estimated to be less than 2% in the center region. The hypothesis (i) is therefore considered to be insufficient to fully explain the observed discrepancies. An important observation to investigate the possibility (ii) is the comparison of the grid "*MIGnh-log-LEGO_N15*" (c) with the grid "*MIGnh-rk4-log-LEGO_N15*" (d) since the two share the same levels distribution but a different design model. It appears that "*MIGnh-rk4-log-LEGO_N15*" gives a roughness significantly closer to the design input than "*MIGnh-log-LEGO_N15*". This observation suggests that the numerical solving of Equation (2) represents an improvement

DOI: 10.13009/EUCASS2022-6178

compared to the McCarthy model. Such observation has to be further justified with new numerically computed grids. Finally, the hypothesis (iii) may be tested by combining the grid with the roughness configuration.

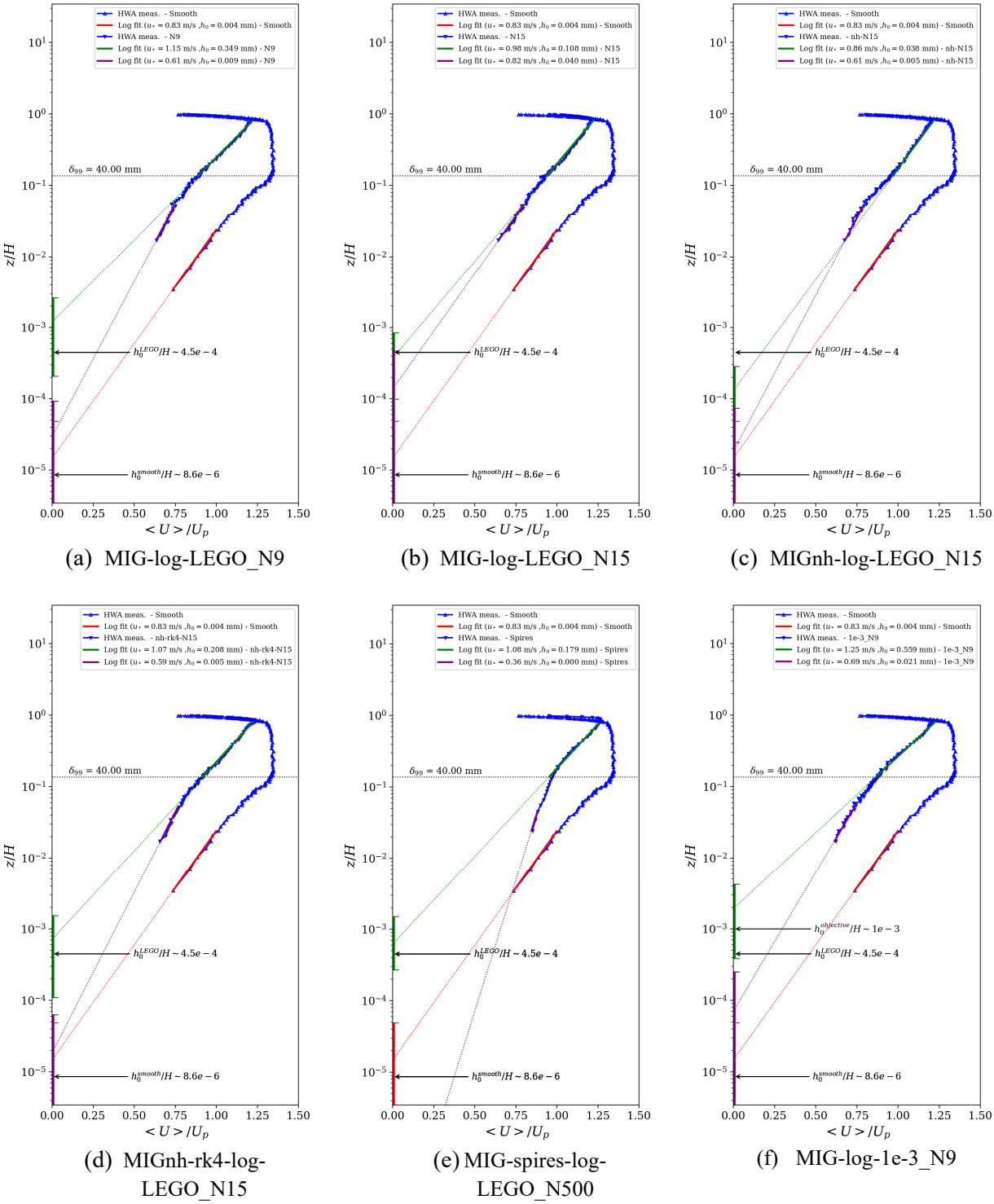

(a) MIG-log-LEGO_N9 (b) MIG-log-LEGO_N15 (c) MIGnh-log-LEGO_N15

(d) MIGnh-rk4-log-LEGO_N15 (e) MIG-spires-log-LEGO_N500 (f) MIG-log-1e-3_N9

Figure 13: Mean longitudinal mean flow velocity profile measured at position $x = 1950\ m$ downstream of the grid/obstacles in **smooth** configuration.

DOI: 10.13009/EUCASS2022-6178

4.2 Combination of grids with roughness

The Figure (14) represents the mean flow profiles downstream of each grid at the same location as the Figure (13) in association with LEGO® baseboard roughness at the wall.

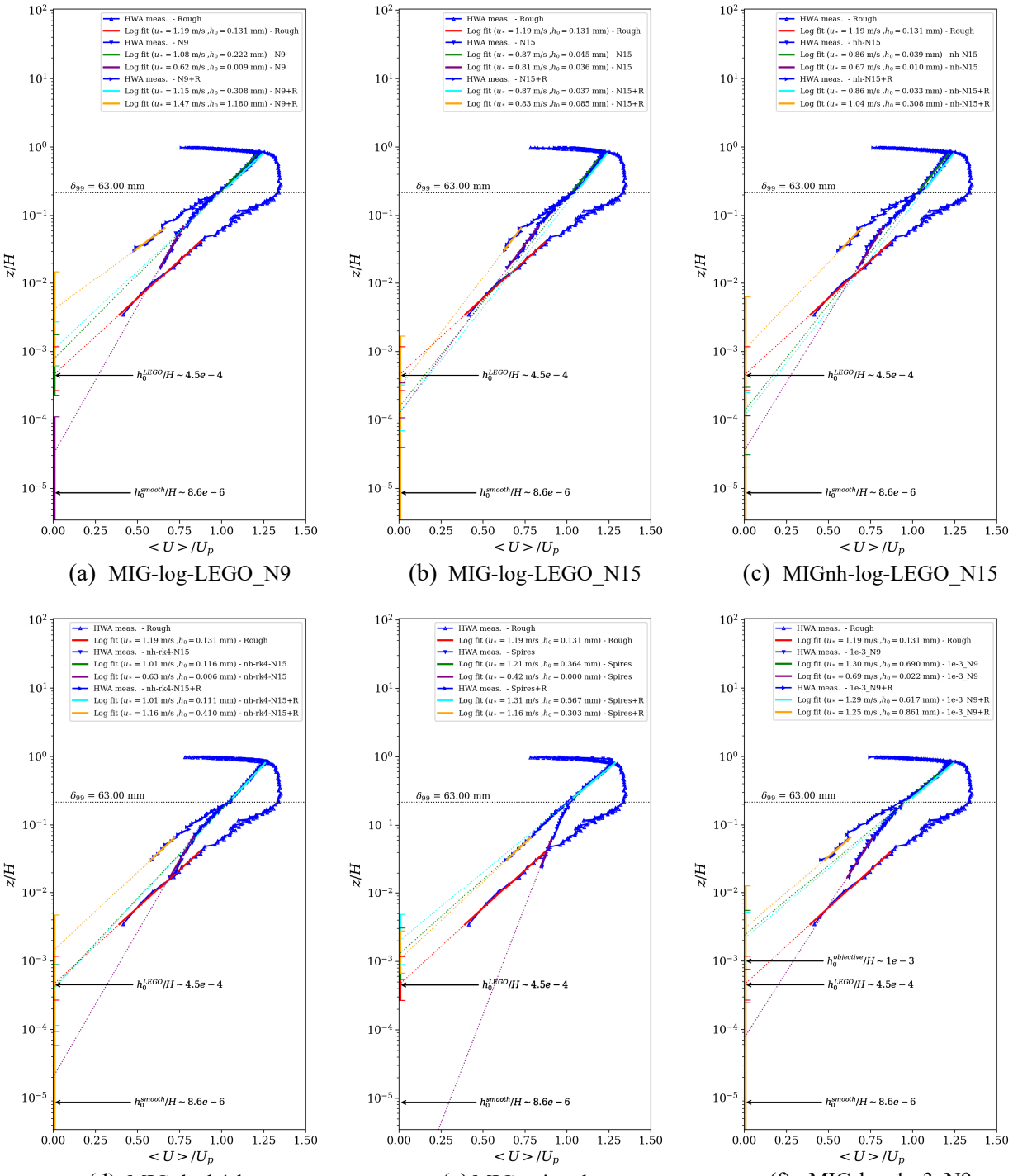

(a) MIG-log-LEGO_N9 (b) MIG-log-LEGO_N15 (c) MIGnh-log-LEGO_N15

(d) MIGnh-rk4-log-LEGO_N15 (e) MIG-spires-log-LEGO_N500 (f) MIG-log-1e-3_N9

Figure 14: Mean longitudinal mean flow velocity profile measured at position $x = 1950\ m$ downstream of the grid/obstacles in smooth and **rough** configurations.

DOI: 10.13009/EUCASS2022-6178

The Figure (14) reveals that roughness has a very low influence above the equivalent boundary layer height growing in no-grid condition. Indeed, the log-law parameters obtained in the center region of the wind tunnel section remain similar to their values without roughness. However, closer to the wall, the roughness does not seem to correct properly the h_0 discrepancy with the design input observed at these altitudes without roughness. Far from having a correction effect, supposedly leading to identical parameters between center region and wall-region, the roughness seems to have a too high decelerating effect. In wall-region, our grid-roughness data are not sufficiently close to the wall to be fully conclusive on the log-law parameters within region. Therefore, new measurements are currently undertaken to better characterize this region. This new database will help quantify the exact influence of the roughness, so that it will be possible to take it into account in the grid design.

Nevertheless, the conclusion is significantly different for "*MIG-spires-log-LEGO_N15*" (Figure (14) -d) where the two flow regions effectively show the same logarithmic parameters. This success is consistent with previous successful passive devices, such as the Irwin (1981) [4] spires-roughness combination. It shows that spires generated using the McCarthy model give satisfactory results in the same way as these previous methods. On the contrary, grids interact in a different way with roughness, probably because of their specific turbulent structure scales and density, which depends on the scales of the grid mesh.

4.3 Turbulence intensity

The streamwise turbulence intensity measured at the location *"IIIT9-Center"* (see Section 3.1) corresponding to *"MIG-nh-rk4-log-LEGO_N15"* (d) and *"MIG-spires-log-LEGO_N500"* (e) are presented in Figure (15). Conclusions with the other grids are similar to the one with *"MIG-nh-rk4-log-LEGO_N15"*. As it was the case for mean flow profiles, the wind tunnel center region (roughly between 0.2H and 0.8H) is very weakly affected by the roughness change. For all the cases, the center-region turbulence is too weak compared to the atmospheric requirements. However, spires appear to produce significant turbulence intensity up to high altitudes. On the contrary, the grid generated flow only shows high turbulence in the wall-affected region, and low intensity (up to 2%) in the grid-affected region. This is consistent with the well-known observation that passive grid-generated turbulence decay faster [2,3], due to smaller turbulence production length scales.

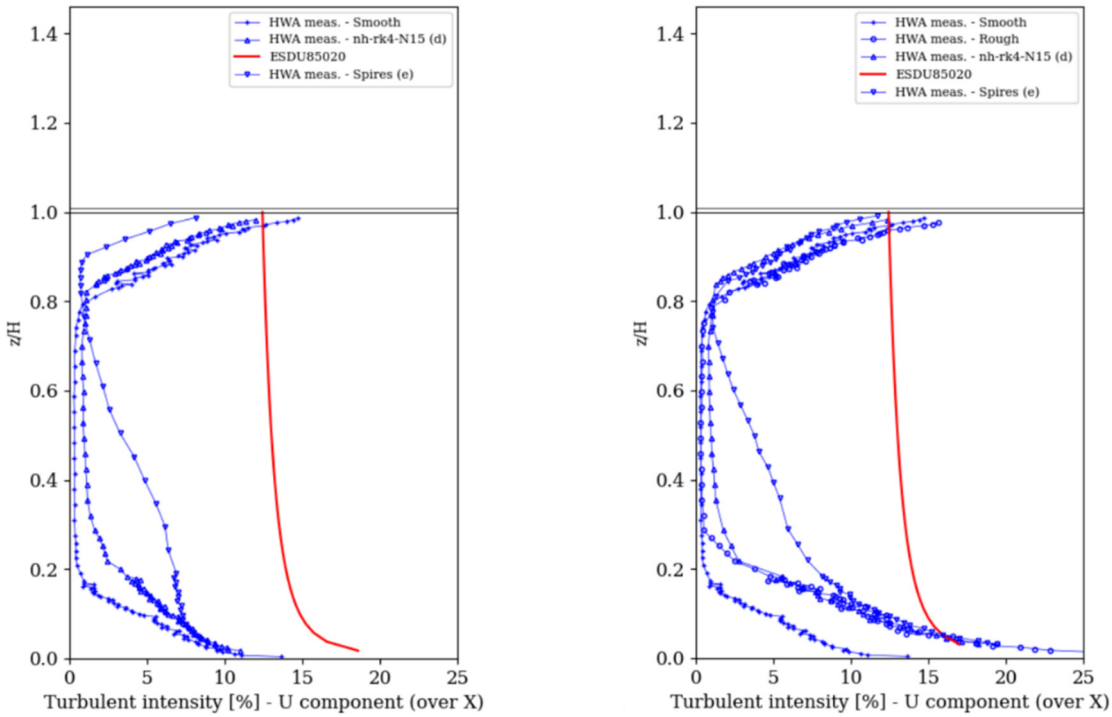

(a) Smooth configuration (b) Rough configuration

Figure 15: Streamwise turbulent intensity measured by HWA in SCL-PIV at the location of the "*IIIT9-Center*" profile. The profiles are compared to the ESDU85020 atmospheric model [27] adapted with the LEGO® Baseboard roughness length.

DOI: 10.13009/EUCASS2022-6178

5. Conclusion & perspectives

This work shows the first investigations undertaken to explore the possibilities of generating a prescribed mean flow representative of atmospheric boundary layer with Multiscale Inhomogeneous Grids (MIGs). The choice of this type of grids is justified by its capacity to tailor turbulence intensity. Before reaching this turbulence control step, the present work is mainly interested in validating the mean flow tailoring by MIGs. Two models are suggested, both depending on the theoretical reasoning explicited by McCarthy (1964). With 6 different grids or obstacles designed using these models, the center vein region is shown to depend mainly on the grid characteristics, showing a good match with the expected mean velocity profiles.

However, the wall-region remain mainly influenced by the wall roughness. Surprisingly, an attempt to reach roughness similarity led to larger discrepancies, except for the "spires" configuration, which shows a very good match with the expected mean flow even within the wall region. This reveals that the geometric differences between grid and spires have a significant influence on the interaction with roughness. This is probably due to the larger vortex structures produced by spires, which enable a coupling of flow layers over a significant range of altitudes (as explained by Cook (1978) [3]). Downstream of passive grids, turbulent structures scale with the mesh size (e.g. [28,29]) and are probably too small to produce the same effect as spires.

This observation motivates the development of prediction model for the integral length scale downstream of MIGs, in order to control more precisely the structures size. This work is currently in progress. Moreover, observation of the turbulent structures past MIGs will be made possible using a stereo-PIV setup. The turbulence intensity prediction model currently in development will benefit from both these integral length scales prediction and these turbulent structures observations.

References

[1] J. Counihan, "An improved method of simulating an atmospheric boundary layer in a wind tunnel," *Atmospheric Environment (1967)*, vol. 3, no. 2 : 197–200, 1969.
[2] J. C. R. Hunt and H. Fernholz, "Wind-tunnel simulation of the atmospheric boundary layer: a report on Euromech 50," *Journal of Fluid Mechanics*, vol. 70, no. 3, pp. 543–559, Aug. 1975.
[3] N. J. Cook, "Wind-tunnel simulation of the adiabatic atmospheric boundary layer by roughness, barrier and mixing-device methods," *Journal of Wind Engineering and Industrial Aerodynamics*, vol. 3, no. 2, pp. 157–176, Jan. 1978.
[4] H. P. A. H. Irwin, "The design of spires for wind simulation," *Journal of Wind Engineering and Industrial Aerodynamics*, vol. 7, no. 3, pp. 361–366, May 1981.
[5] R. J. Hearst and B. Ganapathisubramani, "Tailoring incoming shear and turbulence profiles for lab-scale wind turbines," *Wind Energy*, vol. 20, no. 12, pp. 2021–2035, Dec. 2017.
[6] J. E. Cermak, "Laboratory Simulation of the Atmospheric Boundary Layer," *AIAA Journal*, vol. 9, no. 9, pp. 1746–1754, Sep. 1971.
[7] R. Avissar, M. D. Moran, G. Wu, R. N. Meroney, and R. A. Pielke, "Operating ranges of mesoscale numerical models and meteorological wind tunnels for the simulation of sea and land breezes," *Boundary-Layer Meteorol*, vol. 50, no. 1, pp. 227–275, Mar. 1990.
[8] J. Armitt and J. Counihan, "The simulation of the atmospheric boundary layer in a wind tunnel," *Atmospheric Environment (1967)*, vol. 2, no. 1, pp. 49–71, Jan. 1968.
[9] M. Jensen and N. Franck, "Model-scale tests in turbulent wind," 1963.
[10] A. S. Monin and A. M. Obukhov, "Basic laws of turbulent mixing in the surface layer of the atmosphere," *Tr. Akad. Nauk. SSSR Geophiz. Inst.*, vol. 24, no. 151, pp. 163–187, 1954.
[11] J. C. Kaimal and J. J. Finnigan, *Atmospheric Boundary Layer Flows: Their Structure and Measurement*. Oxford, New York: Oxford University Press, 1994.
[12] M. R. Raupach, R. A. Antonia, and S. Rajagopalan, "Rough-Wall Turbulent Boundary Layers," *Applied Mechanics Reviews*, vol. 44, no. 1, pp. 1–25, Jan. 1991.
[13] J. Wieringa, "Updating the Davenport roughness classification," *Journal of Wind Engineering and Industrial Aerodynamics*, vol. 41, no. 1, pp. 357–368, Oct. 1992.
[14] A. Davenport, C. Grimmond, T. Oke, and J. Wieringa, "Estimating the roughness of cities and sheltered country," *15th conference on probability and statistics in the atmospheric sciences/12th conference on applied climatology, Ashville, NC, American Meteorological Society*, pp. 96–99, Jan. 2000.
[15] A. G. Davenport and N. Isyumov, "The application of a the boundary layer wind tunnel to the prediction of wind loading," 1967.

DOI: 10.13009/EUCASS2022-6178

[16] J. Counihan, “Further measurements in a simulated atmospheric boundary layer,” *Atmospheric Environment (1967)*, vol. 4, no. 3, pp. 259–275, May 1970.
[17] H. P. A. H. Irwin, “Design and use of spires for natural wind simulation,” *Laboratory Technical Report (National Research Council of Canada. National Aeronautical Establishment. Low Speed Aerodynamics Laboratory)*, p. 65 p., Aug. 1979.
[18] S. Zheng, P. J. K. Bruce, J. M. R. Graham, and J. C. Vassilicos, “Weakly sheared turbulent flows generated by multiscale inhomogeneous grids,” *Journal of Fluid Mechanics*, vol. 848, pp. 788–820, Aug. 2018
[19] J. H. McCarthy, “Steady flow past non-uniform wire grids,” *Journal of Fluid Mechanics*, vol. 19, no. 4, pp. 491–512, Aug. 1964.
[20] G. I. Taylor, G. K. Batchelor, H. L. Dryden, and G. B. Schubauer, “THE EFFECT OF WIRE GAUZE ON SMALL DISTURBANCES IN A UNIFORM STREAM,” Q J Mechanics Appl Math, vol. 2, no. 1, pp. 1–29, Jan. 1949
[21] P. R. Owen and H. K. Zienkiewicz, “The production of uniform shear flow in a wind tunnel,” *Journal of Fluid Mechanics*, vol. 2, no. 6, pp. 521–531, Aug. 1957.
[22] J. W. Elder, “Steady flow through non-uniform gauzes of arbitrary shape,” *Journal of Fluid Mechanics*, vol. 5, no. 3, pp. 355–368, Apr. 1959.
[23] U. Karnik and S. Tavoularis, “Generation and manipulation of uniform shear with the use of screens,” *Experiments in Fluids*, vol. 5, no. 4, pp. 247–254, Jul. 1987.
[24] K. E. G. Wieghardt, “On the Resistance of Screens,” *Aeronautical Quarterly*, vol. 4, no. 2, pp. 186–192, Aug. 1953.
[25] W. G. Cornell, “Losses of flow normal to plane screens,” *Trans. ASME*, vol. 80, no. 4, pp. 791–799, 1958.
[26] P. E. Roach, “The generation of nearly isotropic turbulence by means of grids,” *International Journal of Heat and Fluid Flow*, vol. 8, no. 2, pp. 82–92, Jun. 1987.
[27] ESDU 85020, “Characteristics of atmospheric turbulence near the ground - Part II: singlepoint data for strong winds (neutral atmosphere).” Engineering Sciences Data Unit, 1985.
[28] P. C. Valente and J. C. Vassilicos, “The decay of turbulence generated by a class of multiscale grids,” *Journal of Fluid Mechanics*, vol. 687, pp. 300–340, Nov. 2011.
[29] J. Nedić and S. Tavoularis, “Energy dissipation scaling in uniformly sheared turbulence,” *Phys. Rev. E*, vol. 93, no. 3, p. 033-115, Mar. 2016.